PNAS RESEARCH ARTICLE | EARTH, ATMOSPHERIC, AND PLANETARY SCIENCES

Assessing effective radiative forcing from aerosol–cloud interactions over the global ocean

Casey J. Wall[a,1,2], Joel R. Norris[a], Anna Possner[b], Daniel T. McCoy[c], Isabel L. McCoy[d,e], and Nicholas J. Lutsko[a]

Edited by Kerry Emanuel, Massachusetts Institute of Technology, Cambridge, MA; received June 17, 2022; accepted September 13, 2022

How clouds respond to anthropogenic sulfate aerosols is one of the largest sources of uncertainty in the radiative forcing of climate over the industrial era. This uncertainty limits our ability to predict equilibrium climate sensitivity (ECS)—the equilibrium global warming following a doubling of atmospheric CO_2. Here, we use satellite observations to quantify relationships between sulfate aerosols and low-level clouds while carefully controlling for meteorology. We then combine the relationships with estimates of the change in sulfate concentration since about 1850 to constrain the associated radiative forcing. We estimate that the cloud-mediated radiative forcing from anthropogenic sulfate aerosols is -1.11 ± 0.43 W m^{-2} over the global ocean (95% confidence). This constraint implies that ECS is likely between 2.9 and 4.5 K (66% confidence). Our results indicate that aerosol forcing is less uncertain and ECS is probably larger than the ranges proposed by recent climate assessments.

climate change | aerosol radiative forcing | aerosol–cloud interactions | climate sensitivity

Significance

A key challenge of climate science is to predict long-term global warming that will result from anthropogenic emissions of greenhouse gases. Long-term warming can be inferred from the historical climate record, but this line of evidence is complicated by the fact that anthropogenic aerosols also contribute to observed climate trends. Here, we use satellite observations to quantify relationships between aerosols and clouds over the global ocean. These relationships reduce uncertainty in climate forcing by anthropogenic aerosols and imply that global temperature is probably more sensitive to changes in greenhouse gas concentrations than predicted by recent climate assessments.

Emissions from industrial activities change the composition of the atmosphere, thereby exerting a radiative forcing on Earth's climate. One important component of the forcing arises from emissions of hygroscopic aerosols and precursor gases that increase the number of cloud-condensation nuclei (CCN) in the atmosphere. Clouds respond to this perturbation by immediately forming smaller but more numerous droplets and then adjusting in ways that can change cloud amount or total water content. The perturbation to the radiation balance at the top of the atmosphere that results from the immediate cloud response and subsequent cloud adjustment is termed the effective radiative forcing from aerosol–cloud interactions (ERF_{aci}). Global-mean ERF_{aci} is dominated by anthropogenic sulfate aerosols (1, 2), which produce a potentially large but highly uncertain cooling effect by modifying low-level clouds (3, 4). This uncertainty limits our ability to constrain equilibrium climate sensitivity (ECS) (5, 6).

One major source of uncertainty of ERF_{aci} stems from the difficulty of quantifying aerosol–cloud interactions using observations. This task is challenging because meteorological variations can give rise to correlations between aerosols and clouds that do not represent a direct causal relationship between the two (7–9). Here, we address this challenge by implementing a method that removes confounding meteorological factors from observed sulfate–low-cloud relationships. This facilitates strong observational constraints on ERF_{aci} and ECS.

Cloud-Controlling Factor Analysis

We relate sulfate aerosol concentration to low-cloud properties using cloud-controlling factor analysis (10). This framework has been used extensively to constrain cloud–climate feedbacks (11, 12), but it has not been used to constrain ERF_{aci} before. The method assumes that anomalies of a generic low-cloud property C can be expressed as a linear combination of seven local environmental predictor variables x_i:

$$C' \approx \sum_{i=1}^{7} \frac{\partial C}{\partial x_i} x_i', \quad [1]$$

where primes denote monthly anomalies from the climatological seasonal cycle and low clouds are defined as having cloud-top pressure (CTP) greater than 680 hPa. The first six x_i terms include sea-surface temperature (SST), estimated inversion strength (EIS) at the top of the planetary boundary layer (13), horizontal advection across a surface–temperature gradient, relative humidity at 700 hPa, vertical velocity at 700 hPa, and near-surface wind speed. These terms encapsulate all proposed mechanisms of large-scale meteorological controls on marine low clouds (10). The final x_i term is the base-10 logarithm of sulfate aerosol mass concentration at 910 hPa, $\log_{10} s$. This term has logarithmic form because the logarithm of sulfate mass concentration is approximately

Author affiliations: [a]Scripps Institution of Oceanography, University of California San Diego, La Jolla, CA 92093; [b]Institute for Atmospheric and Environmental Sciences, Goethe University Frankfurt, Frankfurt, 60438, Germany; [c]Department of Atmospheric Sciences, University of Wyoming, Laramie, WY 82071; [d]Rosenstiel School of Marine and Atmospheric Science, University of Miami, Miami, FL 33149; and [e]Cooperative Programs for the Advancement of Earth System Science, University Corporation for Atmospheric Research, Boulder, CO 80307

Author contributions: C.J.W. and J.R.N. designed research; C.J.W. performed research; C.J.W. analyzed data; A.P., D.T.M., I.L.M., and N.J.L. contributed ideas; and C.J.W., J.R.N., A.P., D.T.M., I.L.M., and N.J.L. wrote the paper.

The authors declare no competing interest.

This article is a PNAS Direct Submission.

[1]To whom correspondence may be addressed. Email: casey.wall@geo.uio.no.

[2]Present address: Department of Geosciences, University of Oslo, 0316 Oslo, Norway.

This article contains supporting information online at http://www.pnas.org/lookup/suppl/doi:10.1073/pnas.2210481119/-/DCSupplemental.

Published November 7, 2022.

proportional to the logarithm of cloud-droplet number concentration (14), and the logarithm of cloud-droplet number concentration is approximately proportional to cloud albedo at regional scales (1, 15). Furthermore, the 910-hPa level is used rather than the surface because conditions at 910 hPa are a better indicator of CCN concentration near the cloud base (16). Thus, $\partial C/\partial \log_{10} s$ represents the aerosol–cloud relationships that are most relevant to $\mathrm{ERF}_{\mathrm{aci}}$.

We estimate $\partial C/\partial x_i$ by applying multilinear regression to monthly satellite and reanalysis data. Low-cloud properties are obtained from the Clouds and the Earth's Radiant Energy System (CERES) (17) and Moderate Resolution Imaging Spectroradiometer (MODIS) (18) satellite datasets, and the x_i terms are calculated from the Modern-Era Retrospective Analysis for Research and Applications version 2 reanalysis (MERRA-2) (19, 20). We select ocean-covered grid boxes, remove the climatological seasonal cycle and linear trend from all variables, and spatially average the anomalies over a $5° \times 5°$ grid. We then regress C' against the x_i' terms at each grid box. The regression coefficients for $\partial C/\partial \log_{10} s$ represent the sensitivity of low clouds to local anomalies of $\log_{10} s$ with all of the meteorological predictors held constant. This method improves upon previous observational estimates of aerosol–cloud interactions by comprehensively controlling for meteorology.

Quantifying Aerosol–Cloud Interactions

We first look for evidence of aerosol–cloud interactions in the relationship between sulfate concentration and cloud-droplet effective radius, r_e. The number density of CCN usually controls the number density of cloud droplets in the marine boundary layer, so larger sulfate concentration is expected to coincide with smaller but more numerous droplets (21). Indeed, the CERES and MODIS observations both show that r_e becomes significantly smaller with increasing sulfate concentration over most of the global ocean (Fig. 1 *A* and *B*). Two exceptions occur in small areas of the Arabian Sea and the northeast Atlantic Ocean, where the opposite relationship is observed. However, these positive $\partial \log_{10} r_e/\partial \log_{10} s$ estimates are not found in other MODIS r_e retrievals, suggesting that they may be artifacts from heavy dust loading in these areas (*SI Appendix*, *SI Text* and Fig. S1) (22, 23). Besides these exceptions, the observations robustly show that larger sulfate concentration is associated with smaller cloud droplets.

The sulfate-induced change in r_e can subsequently modify cloud processes in ways that change low-cloud fraction, L_n, or liquid-water path (LWP). For instance, cloudy air that is polluted with anthropogenic CCN will form smaller cloud droplets, which are more susceptible to evaporation when entrainment occurs. Small droplets that reach the cloud-top entrainment zone also sediment more slowly, so they are more likely to be exposed to entrained air. These mechanisms increase cloud evaporation and reduce LWP (24, 25). Other adjustment mechanisms may also occur when precipitating clouds are exposed to polluted air. For instance, CCN pollution can produce smaller cloud droplets that coalesce into raindrops more slowly. This can deepen precipitating clouds and increase detrainment into attached stratiform-cloud elements (26–28). In some cases, pollution may suppress precipitation entirely. This can change major characteristics of the cloud field, such as the mesoscale cellular structure (29, 30). Cloud adjustments may also feed back on the sulfate

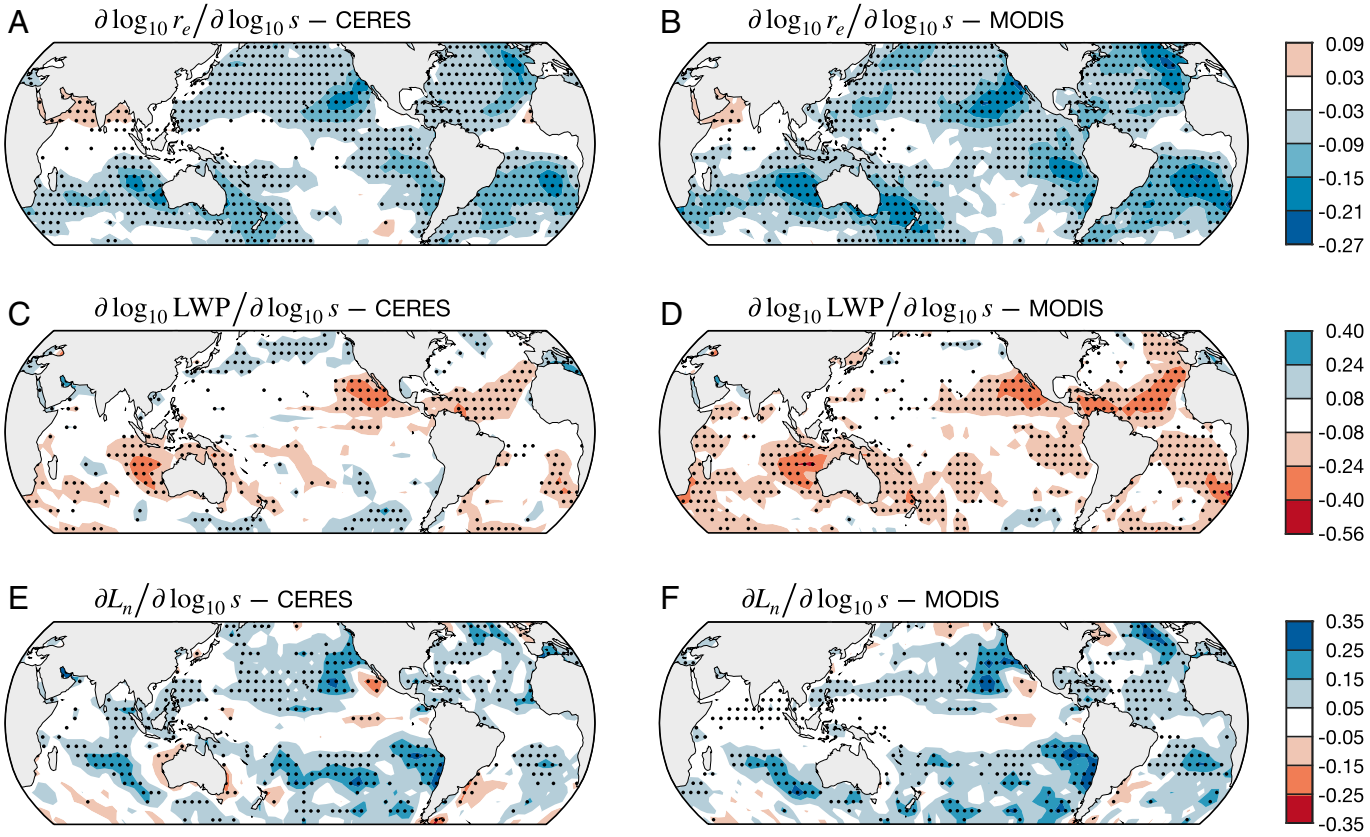

Fig. 1. Relationships between low-cloud properties and local anomalies of $\log_{10} s$. Linear regression coefficients are plotted for (*A* and *B*) $\partial \log_{10} r_e/\partial \log_{10} s$, (*C* and *D*) $\partial \log_{10} \mathrm{LWP}/\partial \log_{10} s$, and (*E* and *F*) $\partial L_n/\partial \log_{10} s$, where r_e is the liquid-cloud effective radius, LWP is the liquid water path, and L_n is the low-cloud fraction. Cloud observations are from (*A*, *C*, and *E*) CERES and (*B*, *D*, and *F*) MODIS. Stippling indicates regression coefficients that are significantly different from zero at the 95% confidence level. Blue colors indicate cloud anomalies that cause more SW reflection to space and vice versa for red colors.

concentration by changing the rates of sulfate removal by precipitation or sulfate production by chemical oxidation of SO_2 dissolved in cloud droplets (31–34). All of these mechanisms could contribute to the observed aerosol–cloud relationships, and their relative importance could vary from one location to another.

We look for evidence of cloud-adjustment mechanisms in the relationships among LWP, L_n, and sulfate concentration. First, we find that larger sulfate concentration is associated with smaller LWP in many locations (Fig. 1 *C* and *D*). This relationship is especially strong in the semipermanent stratocumulus regions of the subtropics and in areas directly downwind. These regions contain a large proportion of stratiform clouds (35–38), suggesting that stratiform clouds may be especially sensitive to aerosol-driven changes in evaporation, sedimentation, and entrainment (24, 25). The $\partial \log_{10}\mathrm{LWP}/\partial \log_{10} s$ relationship is mostly insignificant in other regions of the tropics and subtropics, and it varies spatially in the midlatitudes. Furthermore, larger sulfate concentration is associated with larger L_n in many subtropical and midlatitude locations (Fig. 1 *E* and *F*). The larger L_n occurs in concert with a smaller fraction of precipitating clouds and a smaller ratio of partially cloud-covered pixels to fully cloud-covered pixels (*SI Appendix, SI Text* and Figs. S2 and S3). Thus, compared with the cloud climatology, clouds in high-sulfate environments precipitate less frequently and have smaller perimeter-to-area ratios, implying a larger cloud size (39). These characteristics suggest that sulfate anomalies may be associated with changes in cloud morphology. Such morphological changes could be a consequence of changes in stratiform-cloud area near precipitating clouds or changes in the occurrence of different forms of mesoscale cellular convection (28, 29). Furthermore, sensitivity tests reveal that these relationships cannot be explained by retrieval artifacts (*SI Appendix, SI Text*). These results show that sulfate anomalies change the macroscopic properties of low clouds, or vice versa.

The sulfate–low-cloud relationships suggest that increasing sulfate concentration will coincide with changes in cloud radiative properties, including an albedo enhancement from smaller but more numerous cloud droplets, an albedo enhancement from increasing L_n, and an albedo reduction from decreasing LWP. The overall cloud radiative response is quantified by the shortwave (SW) low-cloud radiative effect R_{SW}, which represents the difference between the true SW flux at the top of the atmosphere and the flux that would occur if low clouds were removed, leaving all else unchanged. We make three estimates of R_{SW} using different cloud retrieval algorithms, different methods for quantifying radiative fluxes, and different filtering choices for pixels that are prone to retrieval bias (*Materials and Methods*). The radiative sensitivities $\partial R_{SW}/\partial \log_{10} s$ are averaged over midlatitude, stratocumulus, and cumulus regimes (Fig. 2*A*). To interpret the results, we also decompose $\partial R_{SW}/\partial \log_{10} s$ into a component associated with changes in cloud amount and a component associated with changes in cloud optical depth and CTP (*Materials and Methods*). The estimates consistently show that low clouds reflect more SW radiation to space as sulfate concentration increases, and the magnitude of $\partial R_{SW}/\partial \log_{10} s$ is largest in stratocumulus clouds and smallest in cumulus clouds (Fig. 2*B*). However, the $\partial R_{SW}/\partial \log_{10} s$ decomposition by cloud properties varies considerably across the three R_{SW} datasets (Fig. 2 *C* and *D*). This discrepancy occurs because different filtering choices for pixels with poor data quality cause offsetting changes in the components of the $\partial R_{SW}/\partial \log_{10} s$ decomposition (*SI Appendix, SI Text*). We note this limitation because it shows that different reasonable choices of data filtering can lead to different interpretations of the underlying causes of cloud radiative sensitivity to sulfate perturbations. Despite this limitation, the estimates of the overall sensitivity $\partial R_{SW}/\partial \log_{10} s$ are consistent across all R_{SW} datasets (Fig. 2*B*). The fact that we arrive at consistent estimates using different datasets and methods gives us confidence that the estimates represent real aerosol–cloud relationships.

Opportunistic Experiments

The observed $\partial R_{SW}/\partial \log_{10} s$ relationships result from coupled aerosol–cloud interactions, in which the direction of causality is not always clear. However, in some "opportunistic experiments," causality is unambiguous (40). These experiments occur when

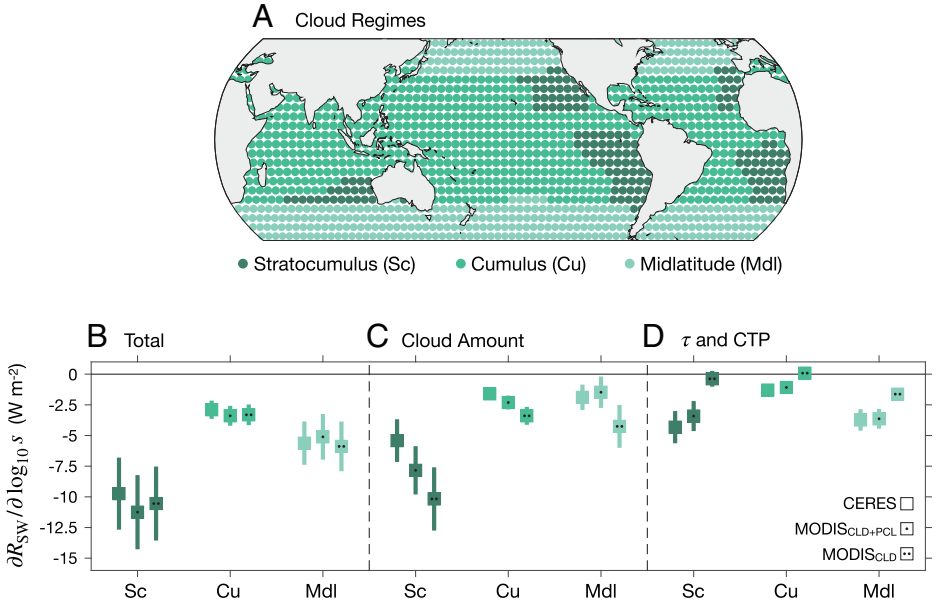

Fig. 2. Relationships between R_{SW} and local anomalies of $\log_{10} s$. (*A*) Locations of stratocumulus (Sc), cumulus (Cu), and midlatitude (Mdl) regimes. (*B*) Regime-average regression coefficients representing $\partial R_{SW}/\partial \log_{10} s$. For each regime, three estimates from different observational datasets and methods are plotted (CERES, MODIS$_{CLD+PCL}$, and MODIS$_{CLD}$) (*Materials and Methods*). (*C* and *D*) Similar to *B* but showing the components of $\partial R_{SW}/\partial \log_{10} s$ that arise from changes in (*C*) cloud amount and (*D*) cloud optical depth (τ) and CTP. Error bars are 95% CIs.

known variations in sulfur emissions cause regional anomalies of $\log_{10}s$. We use these experiments to test if our method can predict how changing sulfur emissions affect clouds at climate-relevant scales.

One opportunistic experiment exists downwind of eastern North America, where efforts to reduce air pollution have decreased sulfur emissions since 2003 (41–43). We examine a 10° latitude by 20° longitude box in the North Atlantic Ocean that experienced a trend in $\log_{10}s$ of -0.08 ± 0.03 decade^{-1} and a trend in R_{SW} of 0.78 ± 0.63 W m^{-2} decade^{-1} during 2003 to 2019 (Fig. 3*A*). These decadal trends are removed prior to the regression analysis, so we test the method based on its ability to predict the R_{SW} trend. We compute changes in the predictor variables between the first eight years (2003 to 2010) and the final eight years (2012 to 2019) of the record, and we input the results to the regression models to predict the change in R_{SW} (Eq. **1** and *Materials and Methods*). The regression method correctly predicts the observed change in regional-mean R_{SW}, and it predicts that sulfate aerosol and meteorology contributed comparable amounts to this change (Fig. 3*B*). The method also correctly predicts the decadal change of R_{SW} downwind of eastern Asia, where significant but smaller trends occurred (*SI Appendix*, *SI Text* and Fig. S4).

Another opportunistic experiment exists near Kīlauea Volcano, Hawai'i, where volcanic eruptions in April to December 2008 and May to August 2018 emitted gaseous SO_2 that ultimately oxidized to form sulfate aerosol (Fig. 3*C*) (44–46). We consider a 20° latitude by 50° longitude box downwind of the volcano, and we test our method by removing data from the eruption periods, performing regression analysis, and using the regression models to predict the average of R'_{SW} during the eruptions (*Materials and Methods*). The method again correctly predicts the regional mean of R'_{SW}, and it attributes this anomaly almost entirely to the increase in sulfate concentration during the eruptions (Fig. 3*D*). Our method thus skillfully predicts large-scale cloud radiative anomalies that are caused by changing sulfur emissions, justifying its use for estimating $\mathrm{ERF_{aci}}$.

Constraining $\mathrm{ERF_{aci}}$

We next use our regression analysis to estimate $\mathrm{ERF_{aci}}$ over the global ocean. Assuming that sulfate aerosols dominate the anthropogenic influence on CCN (1, 2), $\mathrm{ERF_{aci}}$ can be estimated by

$$\mathrm{ERF_{aci}} \approx \left\langle \frac{\partial R_{net}}{\partial \log_{10} s} \Delta \log_{10} s \right\rangle, \qquad [2]$$

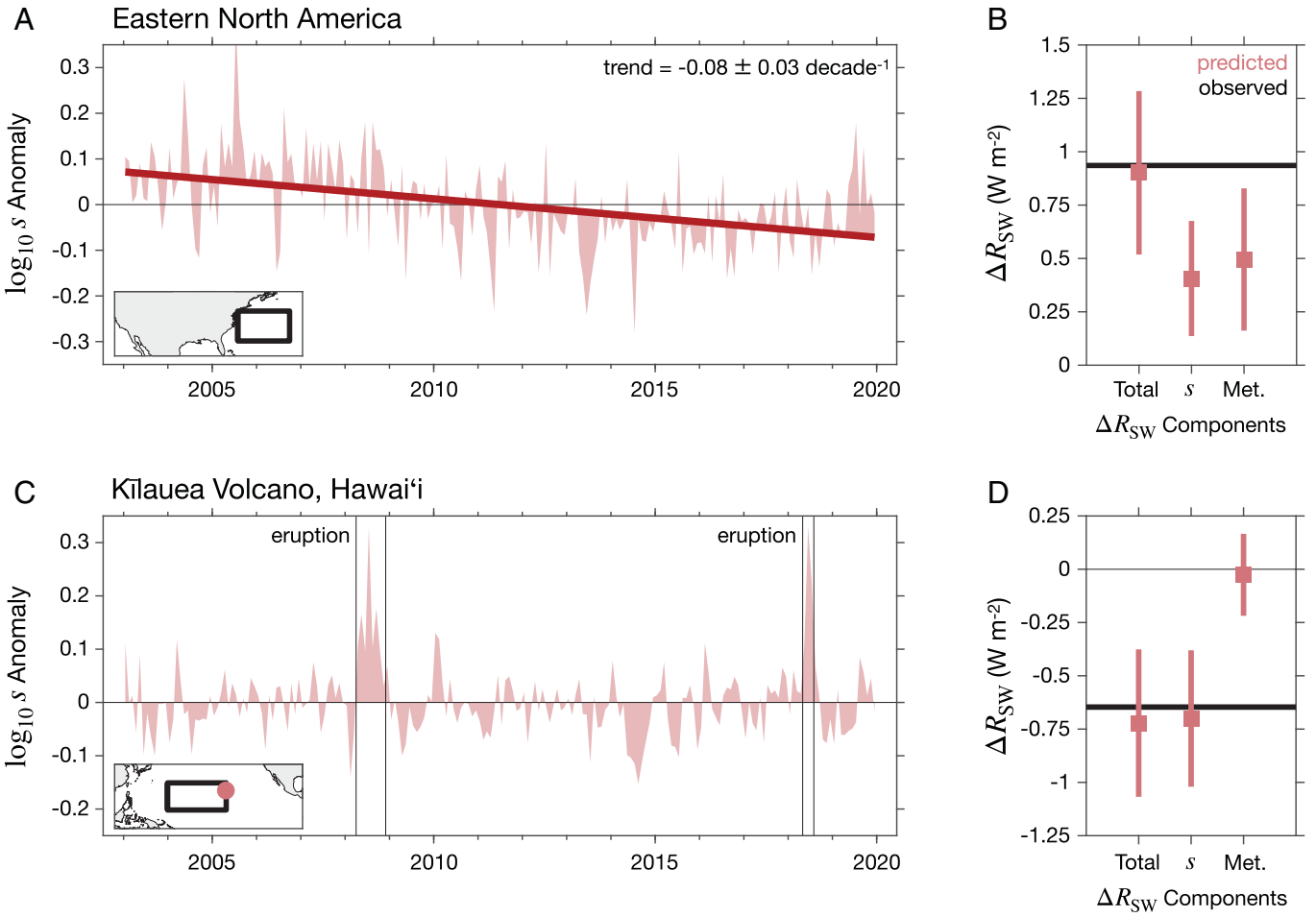

Fig. 3. Method validation using opportunistic experiments with varying sulfur emissions. (*A*) Time series of $\log_{10}s$ anomalies downwind of eastern North America. Data are averaged over the region outlined in *A*, *Inset*. Anomalies in *A* are calculated by removing the climatological seasonal cycle but retaining the long-term linear trend. Shading shows the anomaly time series, and the red line shows the trend. (*B*) Observed and predicted cloud radiative anomalies associated with the opportunistic experiment, ΔR_{SW}. In this case, ΔR_{SW} represents the decadal trend of R_{SW} and is defined as R_{SW} averaged over 2012 to 2019 minus R_{SW} averaged over 2003 to 2010. Predicted values include the total prediction, the contribution from changes in $\log_{10}s$, and the contribution from changes in meteorology (labeled "Total," "*s*," and "Met.," respectively). (*C*) Time series of $\log_{10}s$ anomalies downwind of Kīlauea Volcano, Hawai'i. Data are averaged over the region outlined in *C*, *Inset*. The red dot in *C*, *Inset* shows the location of Kīlauea Volcano, and the vertical lines on the time series show eruptions in 2008 and 2018. (*D*) Similar to *B* except that in this case, ΔR_{SW} is defined as the R_{SW} anomaly averaged over both eruption periods. Uncertainties and error bars are 95% CIs. R_{SW} data are from CERES.

where angle brackets denote a spatial average over the ocean between 55°S and 55°N latitude, R_{net} is the net low-cloud radiative effect, and $\Delta\log_{10}s$ is the change in $\log_{10}s$ between the present-day (2005 to 2014) and preindustrial (1850 to 1859) periods from the output of 20 state-of-the-art global climate models from the Coupled Model Intercomparison Project Phase 6 (CMIP6). Because this estimate relies on model output to determine $\Delta\log_{10}s$, it may be susceptible to model bias from imperfect sulfur emissions or imperfect representations of sulfate processing by clouds. However, anthropogenic sulfur emissions depend primarily on the sulfur content of fuel rather than the conditions of combustion, so they are less uncertain than other forms of air pollution (47). Furthermore, many global climate models simulate recent decadal trends of regional sulfate concentration that are consistent with surface observations (48). The CMIP6 models also simulate expected characteristics of the spatial pattern of $\Delta\log_{10}s$, including a hemispheric asymmetry and especially large values near major industrial areas in Asia and North America (Fig. 4*A*). For these reasons, it seems unlikely that all models in the ensemble share common biases that adversely affect the mean estimate of $\Delta\log_{10}s$. Thus, we proceed using these estimates.

We interpret ERF_{aci} by examining the total value and its decomposition into components associated with changes in different cloud properties. The total ERF_{aci} inferred from CERES observations is -1.11 ± 0.43 W m^{-2} (95% CI). This case is considered to be the best estimate of total ERF_{aci} because it is inferred from satellite retrievals of radiative fluxes, although it closely matches the two MODIS-based estimates (Fig. 4*B* and *Materials and Methods*). The decomposition into a component associated with changes in cloud amount and a component associated with changes in cloud optical depth and CTP varies considerably across our three estimates, but all estimates show that neither component can be neglected (Fig. 4 *C* and *D*). The cloud-amount component can be conservatively bounded above by the most positive value from the CIs of the three estimates in Fig. 4*C*. This approach indicates that there is a 97.5% probability that the contribution of cloud-amount changes to ERF_{aci} is more negative than -0.18 W m^{-2}. Similarly, the cloud optical-depth and CTP component is bounded above by -0.12 W m^{-2}. The upper bound of the optical-depth and CTP component is considerably smaller in magnitude than estimates of cloud brightening from aerosol-driven changes in cloud-droplet size and number concentration (the "Twomey effect") (49–51). Thus, our results do not preclude the possibility that this cloud-brightening effect could be largely offset by cloud-adjustment mechanisms that reduce LWP (Fig. 1). These findings corroborate other observational evidence suggesting that aerosol-driven changes in cloud fraction and perhaps LWP contribute substantially to ERF_{aci} (7, 52–55).

Our near-global estimate of ERF_{aci} covers a domain that includes about 60% of the global surface area and nearly all remote ocean regions, which are especially sensitive to anthropogenic CCN (56). The estimate does not include polar oceans, but these regions make a small contribution to global ERF_{aci} because they cover a relatively small area and experience weak insolation. For these reasons, the near-global estimate should approximately represent the true global average. Indeed, CMIP6 models confirm this expectation (*SI Appendix*, Fig. S5). Thus, we relate global-average ERF_{aci} to domain-average ERF_{aci} with a scalar γ that represents the ratio of the two quantities. We calculate γ using ERF_{aci} estimates from 20 CMIP6 climate models, and we scale the domain-average ERF_{aci} by γ to estimate the global-average ERF_{aci} (*Materials and Methods*).

Adopting terminology from the Intergovernmental Panel on Climate Change (IPCC), our global estimate of ERF_{aci} inferred from CERES observations has a very likely range (90% CI) of

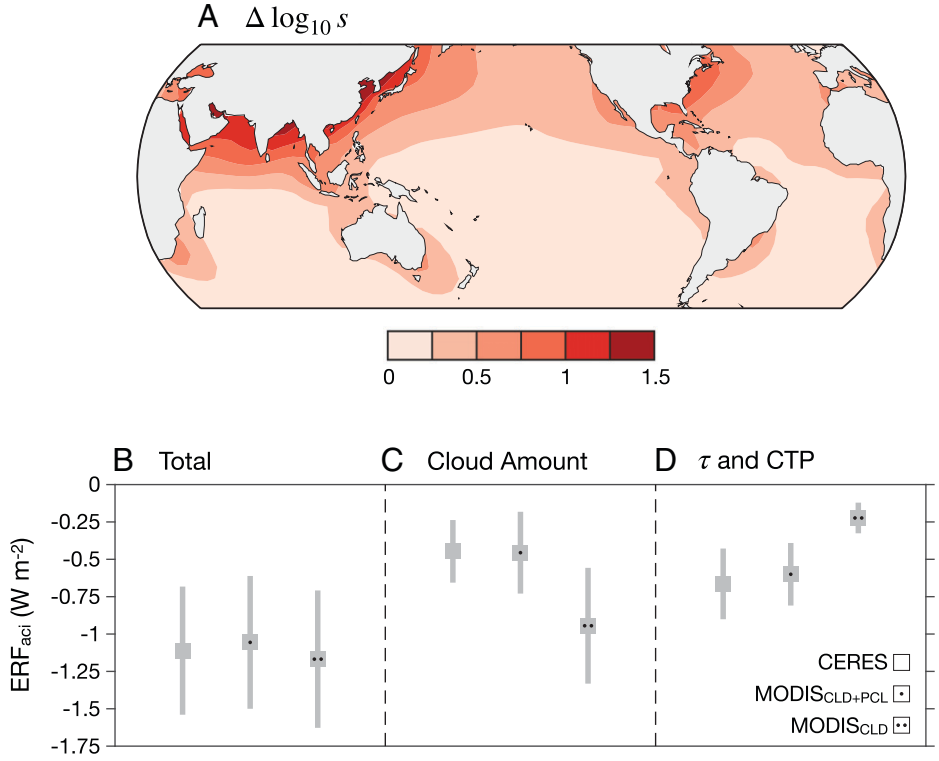

Fig. 4. ERF_{aci} over the global ocean. (*A*) Climate model estimate of the change in $\log_{10}s$ between present-day and preindustrial conditions. The mean from 20 CMIP6 models is plotted. (*B*) Total ERF_{aci} averaged over the ocean between 55°S and 55°N. Three estimates of ERF_{aci} are obtained using different observational datasets and methods (CERES, $MODIS_{CLD+PCL}$, and $MODIS_{CLD}$). (*C* and *D*) Similar to *B* but showing the components of ERF_{aci} that arise from changes in (*C*) cloud amount and (*D*) cloud optical depth (τ) and CTP. Error bars are 95% CIs.

-1.16 ± 0.48 W m^{-2} (Fig. 5*A*). This range is ~30% narrower than the observationally based range proposed by the IPCC Sixth Assessment Report (4) and ~60% narrower than the range proposed by the World Climate Research Program (WCRP) (3). Our estimate lies within the IPCC- and WCRP-assessed ranges, but its probability density is concentrated at relatively large negative values. For instance, we estimate that ERF_{aci} is probably more negative than -0.68 W m^{-2} (95% probability), while the IPCC and WCRP very likely ranges extend up to -0.23 and -0.07 W m^{-2}, respectively. In other words, our results show that ERF_{aci} is less uncertain and potentially larger in magnitude than the ranges proposed by recent climate assessments. Compared with the observational studies that inform these assessments, we control for more confounding meteorological factors and validate our method more thoroughly with opportunistic experiments. Thus, we establish a narrower and more robust constraint on ERF_{aci}.

Implications for Climate Sensitivity

Our constraint on ERF_{aci} indicates that forcing from anthropogenic sulfate aerosols masked a substantial fraction of forcing from greenhouse gases between the present-day and preindustrial periods. This implies that global-mean surface temperature must be relatively sensitive to greenhouse gas forcing to have warmed as much as it did during the twentieth century. We quantify the long-term implications of this result using the metric of ECS, which is defined as the equilibrium change in global-mean surface air temperature following a sustained doubling of atmospheric CO_2 over its preindustrial value. ECS is calculated using a framework developed by the WCRP that incorporates multiple lines of evidence (5). We refine the evidence from the historical climate record by substituting our estimate of ERF_{aci} in place of the original distribution (*Materials and Methods*). This line of evidence constrains the lower bound of ECS (5), so our ERF_{aci} estimate substantially changes the ECS prediction (Fig. 5*B*). We estimate that the likely range of ECS is 2.9 to 4.5 K (66% CI), which is shifted toward larger values relative to the ranges proposed by the WCRP (2.6 to 3.9 K) (5) and the IPCC Sixth Assessment Report (2.5 to 4.0 K) (4). Our central estimate of ECS is also about 0.5 K larger than that of the two assessments. Furthermore, we find that ECS is almost certainly above 2 K (99.9% probability), and it is more likely to be above 4.5 K than predicted by the WCRP (17% probability for our estimate and 7% probability for the WCRP estimate). This means that long-term global warming will probably be more severe than the predictions of the IPCC and the WCRP.

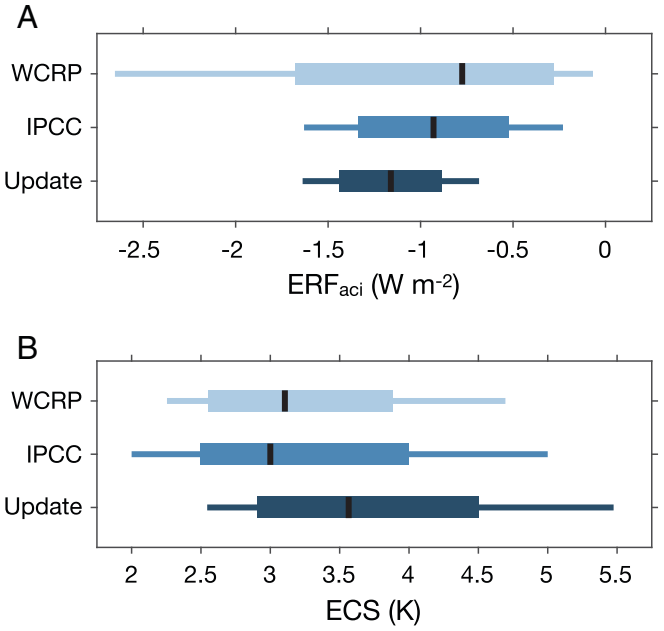

Fig. 5. Estimates of (*A*) global ERF_{aci} and (*B*) ECS from the WCRP, the IPCC Sixth Assessment Report, and our analysis ("Update"). Thin horizontal lines denote 90% CIs, thick horizontal lines denote 66% CIs, and black vertical lines denote central estimates. The central estimates represent the median of the distribution for all cases except the IPCC estimate of ECS. In that case, the central estimate is the reported "best estimate" from the assessment. The IPCC values of ERF_{aci} represent the assessment based on observational evidence alone.

Our ERF_{aci} constraint also has implications for climate change over the twenty-first century. Because sulfate aerosols have a much shorter lifetime in the atmosphere than anthropogenic greenhouse gases, efforts to reduce sulfur emissions could rapidly reduce ERF_{aci} and unmask greenhouse gas forcing. This could cause decadal or centennial warming that would hinder societal aspirations to limit global surface temperature to 1.5 to 2 K above its preindustrial value (57, 58).

Our results demonstrate that careful analysis of satellite observations can robustly constrain estimates of aerosol–cloud interactions and ERF_{aci}. These constraints clarify the underlying causes of historical climate change and refine our estimates of climate sensitivity. Importantly, the constraints imply that recent climate assessments may underestimate the magnitudes of ERF_{aci} and ECS (Fig. 5). This supports the scientific understanding that mitigation efforts targeting aerosol and greenhouse gas forcing are urgently needed to avoid potentially dangerous climate change.

Materials and Methods

Satellite Data, Reanalysis, and CMIP6 Model Output. We analyze monthly gridded satellite observations from the CERES FluxByCldTyp Edition 4.1 dataset (17) and the MODIS Collection 6 MYD08_M3 dataset (18) from 55°S to 55°N during 2003 to 2019. Our primary unit of analysis is a joint histogram of cloud fraction partitioned by cloud optical depth and CTP and a corresponding matrix of the top of atmosphere radiative flux for each histogram bin. We also analyze top of atmosphere clear-sky radiative flux, r_e, and LWP. r_e is defined by the ratio of the third and second moments of the cloud-droplet size distribution, and LWP is defined by the vertically integrated mass of cloud droplets per unit area. We compute the base-10 logarithm of r_e and LWP using daily versions of the CERES and MODIS datasets, then average the results over one-month intervals. These two variables are averaged over pixels identified as liquid clouds. We also use the fractions of low and nonlow clouds, which we define by CTP > 680 hPa and CTP ≤ 680 hPa, respectively. We do not analyze cloud-droplet number concentration because satellite-based estimates of this quantity require strict filtering conditions that can cause small sample sizes or sampling bias, particularly in areas dominated by cumulus clouds (59, 60).

The CERES and MODIS data are retrieved from passive instruments that view the highest cloud in each scene, so nonlow clouds can artificially change the retrieved low-cloud fraction if they obscure low clouds from the satellite view. We address this limitation by defining a metric that is not sensitive to overlying clouds. Let L and U represent the fraction of low and nonlow clouds retrieved by the satellite, respectively. The nonobscured low-cloud fraction, L_n, is defined by $L_n \equiv L/(1-U)$. This metric represents the low-cloud fraction relative to the area that is not obscured by overlying clouds.

We also analyze R_{SW}, which represents the difference between the actual top of atmosphere SW flux and the flux that would occur if low clouds were removed leaving all else unchanged. We estimate R'_{SW} controlling for cloud obscuration effects following the procedure recommended in ref. 10:

$$R'_{SW} = \left(\sum_{p=1}^{P} \sum_{t=1}^{T} \frac{\overline{f_{pt}}}{\overline{L}} \left(\overline{R_{pt}} - \overline{R_{clr}}\right) L'_n (1-\overline{U}) \right) + \left(\sum_{p=1}^{P} \sum_{t=1}^{T} \left(f'_{pt} - \overline{f_{pt}} \frac{L'}{\overline{L}} \right) \left(\overline{R_{pt}} - \overline{R_{clr}}\right) \right),$$

where p runs over the CTP bins for low clouds ($P = 2$ for CERES and $P = 2$ for MODIS), t runs over all optical-depth bins ($T = 6$ for CERES and $T = 8$ for MODIS), f_{pt} is the retrieved cloud fraction in bin (p, t), R_{pt} is top of atmosphere SW flux above clouds in bin $(p,\ t)$, R_{clr} is top of atmosphere SW flux above clear sky, and overbars denote the climatological seasonal cycle. We refer to $\overline{R_{pt}} - \overline{R_{clr}}$ as the cloud radiative kernel. The first term on the right side of this equation represents the R_{SW} anomaly that arises from a change in L_n with no change in the proportion of cloud fraction in each joint CTP and optical-depth bin, and the second term on the right side represents the R_{SW} anomaly that arises from a change in the distribution of optical depth and CTP with no change in L_n. The net radiative effect of low clouds R_{net} is calculated similarly.

To test the robustness of the analysis, we calculate one R'_{SW} estimate using CERES cloud fraction and radiative kernels (CERES case) and two R'_{SW} estimates using MODIS cloud fraction and model-based radiative kernels ($\text{MODIS}_{\text{CLD+PCL}}$ and $\text{MODIS}_{\text{CLD}}$ cases). MODIS kernels are calculated with the Rapid Radiative Transfer Model for Global Climate Models (61) following the method in ref. 62. The $\text{MODIS}_{\text{CLD+PCL}}$ estimate includes partly cloudy pixels in the calculation of cloud fraction, and the $\text{MODIS}_{\text{CLD}}$ estimate does not. We consider these cases separately because partly cloudy pixels are prone to retrieval bias (18). By comparing the three R'_{SW} estimates, we are able to determine if the results are sensitive to the cloud retrieval algorithms, the method for calculating the radiative kernel, or the treatment of partly cloudy pixels. The MODIS-based estimates reproduce monthly variations of the CERES-based estimate with a bias of about +2 to +4% (*SI Appendix*, *SI Text* and Fig. S6).

We also use monthly meteorological fields and sulfate–aerosol mass concentration at 910 hPa from MERRA-2 reanalysis (19, 20). MERRA-2 blends observations and global model simulations to estimate the state of the atmosphere. For sulfate aerosol, bias-corrected observations of total aerosol optical depth are combined with a model that treats the sources, sinks, and chemistry of sulfate and its precursor gases. The data assimilation accounts for aerosol swelling in humid environments and filters out pixels near clouds that are affected by retrieval bias (19). The main limitation of these data is that the total aerosol optical depth is constrained by observations, but aerosol species distributions and vertical profiles are not. Despite this limitation, the estimates of sulfate concentration are strongly correlated with independent satellite retrievals of cloud-droplet number concentration (42).

Finally, we use the output from historical simulations of 20 CMIP6 global climate models. The simulations are run from 1850 through 2014 with realistic emissions of greenhouse gases, aerosols, and aerosol precursor gases. Sulfate mass concentration from the model output is converted to pressure coordinates and then linearly interpolated to the 910-hPa level. The models used in the analysis are listed in *SI Appendix*, Table S1.

Cloud-Controlling Factor Analysis. We extend the cloud-controlling factor analysis of ref. 10 to quantify relationships between sulfate aerosols and low clouds. Let C represent a low-cloud property, such as R_{SW}, R_{net}, $\log_{10}r_e$, $\log_{10}$LWP, or L_n. The cloud-controlling factor framework posits that C' can be approximated by a linear combination of seven environmental predictor variables x_i, including SST, EIS, horizontal advection across a surface–temperature gradient, relative humidity at 700 hPa, vertical velocity at 700 hPa, near-surface wind speed, and $\log_{10}s$ (Eq. **1**). EIS represents the inversion strength at the top of the planetary boundary layer. It is defined as

$$\text{EIS} \equiv (\theta_{700} - \theta_s) - \Gamma_m^{850}(Z_{700} - Z_{LCL}),$$

where θ_{700} is potential temperature at 700 hPa, θ_s is the potential temperature at the surface, Γ_m^{850} is the moist adiabatic lapse rate of potential temperature at 850 hPa, Z_{700} is the height of the 700-hPa pressure level, and Z_{LCL} is the height of the lifting condensation level for an air parcel at the surface (13). Horizontal advection across a surface–temperature gradient, T_{adv}, is defined as

$$T_{adv} \equiv -\boldsymbol{u} \cdot \nabla\text{SST},$$

where $\boldsymbol{u}$ is the horizontal wind vector at 10 m above the surface. All x_i terms are calculated from MERRA-2 data and linearly interpolated to the native $1^\circ \times 1^\circ$ grid of CERES and MODIS. We then select ocean-covered grid boxes, remove the climatological seasonal cycle and linear trend from all variables, and average the anomalies over a $5^\circ \times 5^\circ$ grid. Finally, we regress C' against the x'_i terms separately for each grid box. On average, the regression method explains 42% of the variance of R'_{SW} over the global ocean.

The results of the regression analysis are consolidated by averaging over three cloud regimes. We first identify locations that regularly experience midlatitude weather systems based on the variance of 3-h sea-level pressure. Grid boxes in which the variance exceeds 40 hPa^2 are assigned to a midlatitude regime. The remaining grid boxes are partitioned into stratocumulus and cumulus regimes based on whichever cloud type is observed more frequently in the satellite retrievals of ref. 36. Regression coefficients are spatially averaged over each regime, weighting by ocean area.

Opportunistic Experiments. The first opportunistic experiment tests whether our method can predict the trend of R_{SW} downwind of eastern North America between 30°N to 40°N latitude and 75°W to 55°W longitude during 2003 to 2019 (Fig. 3*A*). Because trends are removed prior to the regression analysis, testing our method based on its ability to predict the R_{SW} trend serves as validation. We begin with gridded R_{SW} and x_i data, in which the climatological seasonal cycle has been removed, but the long-term trend has not. Decadal changes of the variables are estimated at each grid box by subtracting the average during 2003 to 2010 from the average during 2012 to 2019. The x_i changes are then input to the regression models to predict the decadal change of R_{SW}. Finally, the results are spatially averaged over the domain. We find similar results when the domain is expanded by 5° to 10° in latitude and longitude. A similar analysis is performed downwind of eastern Asia in *SI Appendix*, *SI Text* and Fig. S4.

The second opportunistic experiment tests whether our method can predict R'_{SW} downwind of Kīlauea Volcano, Hawai'i, during volcanic eruptions in April to December 2008 and May to August 2018. We consider the region bounded by 5°N to 25°N latitude and 155°W to 155°E longitude, which we define based on visual inspection of the aerosol plumes in MODIS imagery (46). We begin with gridded R'_{SW} and x'_i data, in which the climatological seasonal cycle and long-term trend have both been removed. Regression analysis is first performed using data from outside the eruption periods. We then temporally average x'_i across both eruption periods, and we input the resulting values to the regression models to predict the average of R'_{SW} during the eruptions. Finally, results are spatially averaged over the domain.

Estimating ERF_{aci}. ERF_{aci} is estimated by the product of $\partial R_{net}/\partial\log_{10}s$ and $\Delta\log_{10}s$ (Eq. **2**). Ten-year preindustrial and present-day reference periods are used to remove interannual variability from the estimate of $\Delta\log_{10}s$, and the multimodel mean of $\Delta\log_{10}s$ is used to compute the central estimate of ERF_{aci}. The estimates are then spatially averaged to determine the implications for global climate. Let $\text{ERF}_{\text{aci,d}}$ be the average over the study domain, which includes ocean grid boxes between 55°S and 55°N latitude, and let $\text{ERF}_{\text{aci,g}}$ be the average over the globe. We relate these quantities by

$$\text{ERF}_{\text{aci,g}} = \gamma\text{ERF}_{\text{aci,d}},$$

where γ is a scalar that is estimated from the output of 20 CMIP6 climate models reported in ref. 63 (*SI Appendix*, Table S1). To dampen random errors in individual model realizations (64), we compute the central estimate of γ as the multimodel mean of $\text{ERF}_{\text{aci,g}}$ divided by the multimodel mean of $\text{ERF}_{\text{aci,d}}$. The central estimate of γ computed from this procedure is 1.04. As a sensitivity test, we also estimate γ without using climate model estimates of ERF_{aci}. For this test, we assume that the albedo change associated with ERF_{aci} is approximately the same over the study domain and over the entire globe, which implies that γ is approximately equal to global-mean insolation divided by domain-mean insolation. The central estimate of γ in this case is 0.92. Both cases result in similar estimates of ECS (*SI Appendix*, Fig. S7).

We compare our estimate of $\text{ERF}_{\text{aci,g}}$ with an estimate from a WCRP assessment of aerosol forcing (3) and the observation-based estimate of the IPCC Sixth Assessment Report (4). All estimates represent $\text{ERF}_{\text{aci,g}}$ associated with liquid clouds. Our estimate uses a present-day reference period of 2005 to 2014 and a preindustrial reference period of 1850 to 1859. The WCRP uses a present-day reference period of 2005 to 2015 and a preindustrial reference year of 1850, but previous assessments suggest that this slight difference in reference period will change ERF_{aci} by 0.01 W m^{-2} or less (65). The IPCC uses a present-day reference year of 2014 and a preindustrial reference year of 1750, so we adjust this estimate to make the preindustrial reference period commensurate with the

other two. We do this by subtracting the best estimate of $ERF_{aci,g}$ between 1850 and 1750 (-0.07 W m^{-2}) (66) from the estimate of $ERF_{aci,g}$ between 2014 and 1750 based on observational evidence alone (90% CI: -1.0 ± 0.7 W m^{-2}). The IPCC also estimates $ERF_{aci,g}$ based on modeling evidence alone and modeling and observational evidence combined, but we do not compare with these estimates because they include contributions from changes in ice and mixed-phase clouds.

Uncertainty. Uncertainty in $ERF_{aci,d}$ arises from uncertainty in the regression coefficients representing $\partial R_{net}/\partial \log_{10} s$ and uncertainty in the model estimates of $\Delta \log_{10} s$. We first quantify the component that is attributable to regression coefficient uncertainty. For a particular spatial grid box i, let ε_i represent the half-width of the 95% CI of the grid box mean ERF_{aci}. We estimate ε_i as

$$\varepsilon_i = t_i \sigma_i \sqrt{\frac{N_{\text{nom},i}}{N_{\text{eff},i}}} [\Delta \log_{10} s]_i,$$

where σ_i is the SE of the regression coefficient, $N_{\text{nom},i}$ is the nominal number of temporal degrees of freedom, $N_{\text{eff},i}$ is the effective number of temporal degrees of freedom, square brackets indicate the central estimate of a parameter, and t_i is the critical value of a Student's t distribution at the $(1-\alpha/2)100\%$ significance level using $N_{\text{eff},i} - 8$ degrees of freedom and $\alpha = 0.05$. The ratio $N_{\text{nom},i}/N_{\text{eff},i}$ is estimated as $(1+r)/(1-r)$, where r is the temporal lag-1 autocorrelation of $R'_{net,i}$. The ε_i terms are then combined to account for spatial averaging over the domain. Uncertainty of the domain-average forcing, δ_{obs}, is

$$\delta_{\text{obs}} = \frac{\sqrt{\sum_{i=1}^{N^*_{\text{nom}}} w_i^2 \varepsilon_i^2}}{\sum_{i=1}^{N^*_{\text{nom}}} w_i} \sqrt{\frac{N^*_{\text{nom}}}{N^*_{\text{eff}}}},$$

where N^*_{nom} is the nominal number of spatial degrees of freedom, N^*_{eff} is the effective number of spatial degrees of freedom, and w_i is the ocean area in grid box i. The ratio $N^*_{\text{nom}}/N^*_{\text{eff}}$ is estimated by applying empirical orthogonal function analysis to R'_{net} following equation 5 of ref. 67. $R'_{net,i}$ is multiplied by $\sqrt{w_i}$ prior to the analysis to remove dependencies on the grid geometry (68). The resulting value of δ_{obs} represents the half-width of the 95% CI of $ERF_{aci,d}$ that is attributable to regression-coefficient uncertainty.

The second source of uncertainty arises from intermodel spread in the estimates of $\Delta \log_{10} s$. Because we have estimates from 20 climate models, we construct a 95% CI for $ERF_{aci,d}$ that excludes 1 model and encompasses the range of the other 19. We first calculate 20 estimates of $ERF_{aci,d}$ by multiplying $\Delta \log_{10} s$ from each of the models by $[\partial R_{net}/\partial \log_{10} s]$. The half-width of the CI, $\delta_{\log_{10} s}$, is estimated as the minimum of $|a_1 - a_{19}|/2$ and $|a_2 - a_{20}|/2$, where a_1, a_2, a_{19}, and a_{20} are the smallest, second smallest, second largest, and largest values of the 20 $ERF_{aci,d}$ estimates, respectively. The overall 95% CI is defined by $ERF_{aci,d} \pm \sqrt{\delta^2_{\text{obs}} + \delta^2_{\log_{10} s}}$.

The CI for $ERF_{aci,g}$ includes an additional uncertainty component from the scalar γ that relates $ERF_{aci,d}$ to $ERF_{aci,g}$. γ and $\Delta \log_{10} s$ are both calculated from CMIP6 output, but γ is uncorrelated with global-mean $\Delta \log_{10} s$ across models. For this reason, we treat the uncertainties of γ and $\Delta \log_{10} s$ as independent. Let δ_γ represent the half-width of the 95% CI of $ERF_{aci,g}$ that arises from intermodel spread in the estimates of γ. We construct δ_γ similarly to $\delta_{\log_{10} s}$ such that the CI excludes 1 model and encompasses the range of the other 19. The overall 95% CI is then defined by $ERF_{aci,g} \pm \sqrt{([\gamma]\delta_{\text{obs}})^2 + ([\gamma]\delta_{\log_{10} s})^2 + \delta^2_\gamma}$.

Estimating ECS. We estimate ECS from multiple lines of evidence using a Bayesian framework developed by the WCRP (5). ECS is approximated by effective climate sensitivity, which is calculated by extrapolating the climate response in the first 150 y following an abrupt quadrupling of atmospheric CO_2 over its preindustrial value (69). The "baseline" ECS estimate of the WCRP is computed with the WCRP-assessed range of $ERF_{aci,g}$ plotted in Fig. 5*A* (3). This aerosol-forcing estimate uses reference periods that align with our analysis, so we estimate ECS by repeating the WCRP baseline calculation using our $ERF_{aci,g}$ estimate in place of the original assessed range. The ECS estimates also account for effective radiative forcing from direct aerosol–radiation interactions. We use the original assessed range of this quantity for our ECS estimate.

Data, Materials, and Software Availability. All satellite, reanalysis, and climate model data are publicly available. CERES data were downloaded from the NASA CERES ordering tool (https://ceres.larc.nasa.gov/data/) (70). MODIS and MERRA-2 data were downloaded from NASA Earthdata (https://www.earthdata.nasa.gov/) (71). CMIP6 output was downloaded from the Earth System Grid Federation data portal (https://esgf-node.llnl.gov/projects/cmip6/) (72). The Rapid Radiative Transfer Model for Global Climate Models is available from the Atmospheric & Environmental Research Radiative Transfer Working Group (rtweb.aer.com/rrtm_frame.html) (73). Code for the climate sensitivity analysis of ref. 5 is available from Zenodo [https://zenodo.org/record/3945276#.Yn2tZhPMKlM (74)]. Intermediate data products produced in our analysis, including gridded monthly anomalies and regression coefficients, are available from GitHub [https://github.com/nicklutsko/Radiative_Forcing_Aerosol_Clouds (75)]. All other data are included in the manuscript and *SI Appendix*.

ACKNOWLEDGMENTS. We thank Rob Wood and Mark Webb for helpful discussions and Chris Smith and Mark Zelinka for sharing data. C.J.W. and J.R.N. were supported by NASA Grant 80NSSC18K1020. C.J.W. and N.J.L. were supported by the National Oceanic and Atmospheric Administration Climate Program Office's Modeling, Analysis, Predictions, and Projections Program Grant NA20OAR4310387. A.P. was funded by Federal Ministry of Education and Research "Make Our Planet Great Again–German Research Initiative" Grant 57429624 implemented by the German Academic Exchange Service. D.T.M. was supported by NASA Grant 80NSSC21K2014 and the U.S. Department of Energy's Atmospheric System Research Federal Award DE-SC002227. I.L.M. was supported by the National Oceanic and Atmospheric Administration Climate and Global Change Postdoctoral Fellowship Program administered by the University Corporation for Atmospheric Research's Cooperative Programs for the Advancement of Earth System Science Award NA18NWS4620043B.

1. R. J. Charlson *et al.*, Climate forcing by anthropogenic aerosols. *Science* **255**, 423–430 (1992).
2. B. Stevens, Rethinking the lower bound on aerosol radiative forcing. *J. Clim.* **28**, 4794–4819 (2015).
3. N. Bellouin *et al.*, Bounding global aerosol radiative forcing of climate change. *Rev. Geophys.* **58**, e2019RG000660 (2020).
4. P. Forster *et al.*, "The Earth's energy budget, climate feedbacks, and climate sensitivity" in *Climate Change 2021: The Physical Science Basis. Contribution of Working Group I to the Sixth Assessment Report of the Intergovernmental Panel on Climate Change*. V. Masson-Delmotte *et al.*, Eds. (Cambridge University Press, Cambridge, United Kingdom, 2021), pp. 923–1054.
5. S. C. Sherwood *et al.*, An assessment of Earth's climate sensitivity using multiple lines of evidence. *Rev. Geophys.* **58**, e2019RG000678 (2020).
6. M. O. Andreae, C. D. Jones, P. M. Cox, Strong present-day aerosol cooling implies a hot future. *Nature* **435**, 1187–1190 (2005).
7. E. Gryspeerdt, J. Quaas, N. Bellouin, Constraining the aerosol influence on cloud fraction. *J. Geophys. Res. Atmos.* **121**, 3566–3583 (2016).
8. J. Mülmenstädt, G. Feingold, The radiative forcing of aerosol–cloud interactions in liquid clouds: Wrestling and embracing uncertainty. *Curr. Clim. Change Rep.* **4**, 23–40 (2018).
9. D. T. McCoy, P. Field, H. Gordon, G. S. Elsaesser, D. P. Grosvenor, Untangling causality in midlatitude aerosol-cloud adjustments. *Atmos. Chem. Phys.* **20**, 4085–4103 (2020).
10. R. C. Scott *et al.*, Observed sensitivity of low-cloud radiative effects to meteorological perturbations over the global oceans. *J. Clim.* **33**, 7717–7734 (2020).
11. S. A. Klein, A. Hall, J. R. Norris, R. Pincus, Low-cloud feedbacks from cloud-controlling factors: A review. *Surv. Geophys.* **38**, 1307–1329 (2017).
12. T. A. Myers *et al.*, Observational constraints on low cloud feedback reduce uncertainty of climate sensitivity. *Nat. Clim. Chang.* **11**, 501–507 (2021).
13. R. Wood, C. S. Bretherton, On the relationship between stratiform low cloud cover and lower-tropospheric stability. *J. Clim.* **19**, 6425–6432 (2006).
14. O. Boucher, U. Lohmann, The sulfate-CCN-cloud albedo effect: A sensitivity study with two general circulation models. *Tellus B Chem. Phys. Meterol.* **47**, 281–300 (1995).
15. S. A. Twomey, M. Piepgrass, T. L. Wolfe, An assessment of the impact of pollution on global cloud albedo. *Tellus B Chem. Phys. Meterol.* **36**, 356–366 (1984).
16. D. Painemal *et al.*, Aerosol and cloud microphysics covariability in the northeast Pacific boundary layer estimated with ship-based and satellite remote sensing observations. *J. Geophys. Res. Atmos.* **122**, 2403–2418 (2017).
17. M. Sun *et al.*, Clouds and the Earth's Radiant Energy System (CERES) FluxByCldTyp edition 4 data product. *J. Atmos. Ocean. Technol.* **39**, 303–318 (2022).
18. S. Platnick *et al.*, The MODIS cloud optical and microphysical products: Collection 6 updates and examples from Terra and Aqua. *IEEE Trans. Geosci. Remote Sens.* **55**, 502–525 (2017).
19. C. A. Randles *et al.*, The MERRA-2 aerosol reanalysis, 1980 onward. Part I. System description and data assimilation evaluation. *J. Clim.* **30**, 6823–6850 (2017).
20. R. Gelaro *et al.*, The Modern-Era Retrospective Analysis for Research and Applications, version 2 (MERRA-2). *J. Clim.* **30**, 5419–5454 (2017).
21. D. Rosenfeld *et al.*, Global observations of aerosol-cloud-precipitation-climate interactions. *Rev. Geophys.* **52**, 750–808 (2014).
22. J. I. Brennan, Y. J. Kaufman, I. Koren, R. R. Li, Aerosol-cloud interaction - Misclassification of MODIS clouds in heavy aerosol. *IEEE Trans. Geosci. Remote Sens.* **43**, 911–915 (2005).

23. J. M. Haywood, S. R. Osborne, S. J. Abel, The effect of overlying absorbing aerosol layers on remote sensing retrievals of cloud effective radius and cloud optical depth. *Q. J. R. Meteorol. Soc.* **130**, 779–800 (2004).
24. C. S. Bretherton, P. N. Blossey, J. Uchida, Cloud droplet sedimentation, entrainment efficiency, and subtropical stratocumulus albedo. *Geophys. Res. Lett.* **34**, L03813 (2007).
25. J. D. Small, P. Y. Chuang, G. Feingold, H. Jiang, Can aerosol decrease cloud lifetime? *Geophys. Res. Lett.* **36**, L16806 (2009).
26. R. Pincus, M. B. Baker, Effect of precipitation on the albedo susceptibility of clouds in the marine boundary layer. *Nature* **372**, 250–252 (1994).
27. A. Seifert, T. Heus, R. Pincus, B. Stevens, Large-eddy simulation of the transient and near-equilibrium behavior of precipitating shallow convection. *J. Adv. Model. Earth Syst.* **6**, 513–526 (2015).
28. A. Possner, H. Wang, R. Wood, K. Caldeira, T. P. Ackerman, The efficacy of aerosol-cloud radiative perturbations from near-surface emissions in deep open-cell stratocumuli. *Atmos. Chem. Phys.* **18**, 17475–17488 (2018).
29. D. Rosenfeld, Y. J. Kaufman, I. Koren, Switching cloud cover and dynamical regimes from open to closed Benard cells in response to the suppression of precipitation by aerosols. *Atmos. Chem. Phys.* **6**, 2503–2511 (2006).
30. T. Yamaguchi, G. Feingold, J. Kazil, Stratocumulus to cumulus transition by drizzle. *J. Adv. Model. Earth Syst.* **9**, 2333–2349 (2017).
31. R. Wood, D. Leon, M. Lebsock, J. Snider, A. D. Clarke, Precipitation driving of droplet concentration variability in marine low clouds. *J. Geophys. Res. Atmos.* **117**, D19210 (2012).
32. L. Kang, R. T. Marchand, R. Wood, I. L. McCoy, Coalescence scavenging drives droplet number concentration in southern ocean low clouds. *Geophys. Res. Lett.* **49**, e2022GL097819 (2022).
33. D. A. Hegg, D. S. Covert, H. Jonsson, D. Khelif, C. A. Friehe, Observations of the impact of cloud processing on aerosol light-scattering efficiency. *Tellus B Chem. Phys. Meterol.* **56**, 285–293 (2004).
34. M. O. Andreae, D. Rosenfeld, Aerosol-cloud-precipitation interactions. Part 1. The nature and sources of cloud-active aerosols. *Earth Sci. Rev.* **89**, 13–41 (2008).
35. A. Muhlbauer, I. L. McCoy, R. Wood, Climatology of stratocumulus cloud morphologies: Microphysical properties and radiative effects. *Atmos. Chem. Phys.* **14**, 6695–6716 (2014).
36. G. Cesana, A. D. Del Genio, H. Chepfer, The cumulus and stratocumulus CloudSat-CALIPSO dataset (CASCCAD). *Earth Syst. Sci. Data* **11**, 1745–1764 (2019).
37. S. Rasp, H. Schulz, S. Bony, B. Stevens, Combining crowd-sourcing and deep learning to explore the meso-scale organization of shallow convection. *Bull. Am. Meteorol.* **101**, 1980–1995 (2020).
38. H. Schulz, R. Eastman, B. Stevens, Characterization and evolution of organized shallow convection in the downstream North Atlantic trades. *J. Geophys. Res. Atmos.* **126**, e2021JD034575 (2021).
39. S. Lovejoy, Area-perimeter relation for rain and cloud areas. *Science* **216**, 185–187 (1982).
40. M. W. Christensen *et al.*, Opportunistic experiments to constrain aerosol effective radiative forcing. *Atmos. Chem. Phys.* **22**, 641–674 (2022).
41. N. A. Krotkov *et al.*, Aura OMI observations of regional SO_2 and NO_2 pollution changes from 2005 to 2015. *Atmos. Chem. Phys.* **16**, 4605–4629 (2016).
42. D. T. McCoy *et al.*, Predicting decadal trends in cloud droplet number concentration using reanalysis and satellite data. *Atmos. Chem. Phys.* **18**, 2035–2047 (2018).
43. H. Bai, M. Wang, Z. Zhang, Y. Liu, Synergetic satellite trend analysis of aerosol and warm cloud properties over ocean and its implication for aerosol-cloud interactions. *J. Geophys. Res. Atmos.* **125**, e2019JD031598 (2020).
44. S. Beirle *et al.*, Estimating the volcanic emission rate and atmospheric lifetime of SO_2 from space: A case study for Kīlauea volcano, Hawai'i. *Atmos. Chem. Phys.* **14**, 8309–8322 (2014).
45. C. A. Neal *et al.*, The 2018 rift eruption and summit collapse of Kīlauea Volcano. *Science* **363**, 367–374 (2019).
46. T. Yuan, L. A. Remer, H. Yu, Microphysical, macrophysical and radiative signatures of volcanic aerosols in trade wind cumulus observed by the A-Train. *Atmos. Chem. Phys.* **11**, 7119–7132 (2011).
47. S. J. Smith *et al.*, Anthropogenic sulfur dioxide emissions: 1850-2005. *Atmos. Chem. Phys.* **11**, 1101–1116 (2011).
48. W. Aas *et al.*, Global and regional trends of atmospheric sulfur. *Sci. Rep.* **9**, 953 (2019).
49. O. P. Hasekamp, E. Gryspeerdt, J. Quaas, Analysis of polarimetric satellite measurements suggests stronger cooling due to aerosol-cloud interactions. *Nat. Commun.* **10**, 5405 (2019).
50. I. L. McCoy *et al.*, The hemispheric contrast in cloud microphysical properties constrains aerosol forcing. *Proc. Natl. Acad. Sci. U.S.A.* **117**, 18998–19006 (2020).
51. M. S. Diamond, H. M. Director, R. Eastman, A. Possner, R. Wood, Substantial cloud brightening from shipping in subtropical low clouds. *AGU Adv.* **1**, e2019AV000111 (2020).
52. Y. C. Chen, M. W. Christensen, G. L. Stephens, J. H. Seinfeld, Satellite-based estimate of global aerosol-cloud radiative forcing by marine warm clouds. *Nat. Geosci.* **7**, 643–646 (2014).
53. H. Andersen, J. Cermak, J. Fuchs, R. Knutti, U. Lohmann, Understanding the drivers of marine liquid-water cloud occurrence and properties with global observations using neural networks. *Atmos. Chem. Phys.* **17**, 9535–9546 (2017).
54. D. Rosenfeld *et al.*, Aerosol-driven droplet concentrations dominate coverage and water of oceanic low-level clouds. *Science* **363**, eaav0566 (2019).
55. Y. Chen *et al.*, Machine learning reveals climate forcing from aerosols is dominated by increased cloud cover. *Nat. Geosci.* **15**, 609–614 (2022).
56. K. S. Carslaw *et al.*, Large contribution of natural aerosols to uncertainty in indirect forcing. *Nature* **503**, 67–71 (2013).
57. H. D. Matthews, K. Zickfeld, Climate response to zeroed emissions of greenhouse gases and aerosols. *Nat. Clim. Chang.* **2**, 338–341 (2012).
58. T. Mauritsen, R. Pincus, Committed warming inferred from observations. *Nat. Clim. Chang.* **7**, 652–655 (2017).
59. D. P. Grosvenor *et al.*, Remote sensing of droplet number concentration in warm clouds: A review of the current state of knowledge and perspectives. *Rev. Geophys.* **56**, 409–453 (2018).
60. E. Gryspeerdt *et al.*, The impact of sampling strategy on the cloud droplet number concentration estimated from satellite data. *Atmos. Meas. Tech.* **15**, 3875–3892 (2022).
61. S. A. Clough *et al.*, Atmospheric radiative transfer modeling: A summary of the AER codes. *J. Quant. Spectrosc. Radiat. Transf.* **91**, 233–244 (2004).
62. M. D. Zelinka, S. A. Klein, D. L. Hartmann, Computing and partitioning cloud feedbacks using cloud property histograms. Part I. Cloud radiative kernels. *J. Clim.* **25**, 3715–3735 (2012).
63. C. J. Smith *et al.*, Effective radiative forcing and adjustments in CMIP6 models. *Atmos. Chem. Phys.* **20**, 9591–9618 (2020).
64. P. M. Forster *et al.*, Recommendations for diagnosing effective radiative forcing from climate models for CMIP6. *J. Geophys. Res. Atmos.* **121**, 12,460–12,475 (2016).
65. M. Prather *et al.*, "Annex II: Climate system scenario tables" in *Climate Change 2013: The Physical Science Basis. Contribution of Working Group I to the Fifth Assessment Report of the Intergovernmental Panel on Climate Change*. T. F. Stocker *et al.*, Eds. (Cambridge University Press, Cambridge, United Kingdom, 2013), pp. 1395–1446.
66. F. J. Dentener, B. Hall, C. Smith, "Annex III: Tables of historical and projected well-mixed greenhouse gas mixing ratios and effective radiative forcing of all climate forcers" in *Climate Change 2021: The Physical Science Basis. Contribution of Working Group I to the Sixth Assessment Report of the Intergovernmental Panel on Climate Change.* V. Masson-Delmotte *et al.*, Eds. (Cambridge University Press, Cambridge, United Kingdom, 2021), pp. 2139–2152.
67. C. S. Bretherton, M. Widmann, V. P. Dymnikov, J. M. Wallace, I. Blade, Effective number of degrees of freedom of a spatial field. *J. Clim.* **12**, 1990–2009 (1999).
68. G. R. North, T. L. Bell, R. F. Cahalan, Sampling errors in the estimation of empirical orthogonal functions. *Mon. Weather Rev.* **7**, 669–706 (1982).
69. J. M. Gregory *et al.*, A new method for diagnosing radiative forcing and climate sensitivity. *Geophys. Res. Lett.* **31**, L03205 (2004).
70. NASA, CERES Data Products. https://ceres.larc.nasa.gov/data/. Accessed 17 October 2022.
71. NASA, EARTHDATA. https://www.earthdata.nasa.gov/. Accessed 17 October 2022.
72. US Department of Energy, Lawrence Livermore National Laboratory, World Climate Research Program (WCRP), WCRP Coupled Model Intercomparison Project (Phase 6). https://esgf-node.llnl.gov/projects/cmip6/. Accessed 17 October 2022.
73. The Rapid Radiative Transfer Model. The Atmospheric & Environmental Research Radiative Transfer Working Group. RRTM (Stand-Alone Model) / RRTMG (GCM Applications). http://rtweb.aer.com/rrtm_frame.html. Accessed 17 October 2022.
74. M. Webb, Code and Data for WCRP Climate Sensitivity Assessment. Zenodo. https://zenodo.org/record/3945276#.Yn2tZhPMKIM. Accessed 14 July 2020.
75. N. J. Lutsko *et al.*, Assessing effective radiative forcing from aerosol–cloud interactions over the global ocean. GitHub. https://github.com/nicklutsko/Radiative_Forcing_Aerosol_Clouds. Accessed 8 August 2022.